




# Hybrid models of chemotaxis with application to leukocyte migration

Hannah Lu<sup>1</sup> · Kimoon Um<sup>1</sup> · Daniel M. Tartakovsky<sup>1</sup> 

Received: 8 May 2020 / Revised: 24 August 2020 / Accepted: 14 February 2021

© The Author(s), under exclusive licence to Springer-Verlag GmbH, DE part of Springer Nature 2021

## Abstract

Many chemical and biological systems involve reacting species with vastly different numbers of molecules/agents. Hybrid simulations model such phenomena by combining discrete (e.g., agent-based) and continuous (e.g., partial differential equation- or PDE-based) descriptors of the dynamics of reactants with small and large numbers of molecules/agents, respectively. We present a stochastic hybrid algorithm to model a stage of the immune response to inflammation, during which leukocytes reach a pathogen via chemotaxis. While large numbers of chemoattractant molecules justify the use of a PDE-based model to describe the spatiotemporal evolution of its concentration, relatively small numbers of leukocytes and bacteria involved in the process undermine the veracity of their continuum treatment by masking the effects of stochasticity and have to be treated discretely. Motility and interactions between leukocytes and bacteria are modeled via random walk and a stochastic simulation algorithm, respectively. Since the latter assumes the reacting species to be well mixed, the discrete component of our hybrid algorithm deploys stochastic operator splitting, in which the sequence of the diffusion and reaction operations is determined autonomously during each simulation step. We conduct a series of numerical experiments to ascertain the accuracy and computational efficiency of our hybrid simulations and, then, to demonstrate the importance of randomness for predicting leukocyte migration and fate during the immune response to inflammation.

---

This work was supported in part by Air Force Office of Scientific Research under award FA9550-18-1-0474.

---

✉ Daniel M. Tartakovsky  
tartakovsky@stanford.edu

Hannah Lu  
hannahlu@stanford.edu

Kimoon Um  
kimoon.um@gmail.com

<sup>1</sup> Department of Energy Resources Engineering, Stanford University, 367 Panama Street, Stanford, CA 94305, USA

**Keywords** Multiscale · Continuum-discrete · Hybrid · Bacteria · Inflammation

**Mathematics Subject Classification** 92C17 · 60G50 · 35K57

## 1 Introduction

Two mathematical frameworks, discrete and continuous, are routinely used to model kinetics of complex (bio)chemical systems. The discrete framework is based on the chemical master equation (Munsky and Khammash 2006; Gillespie 1992); it is invoked when the number of molecules of reacting species is relatively small, so that stochastic fluctuations in local concentrations become pronounced. This randomness is a key feature of many biological processes, e.g., gene expression (Bravi and Longo 2015), development of neural networks (Changeux and Danchin 1976), and Darwinian selection (Darwin 1859). The continuous framework consists of differential equations describing temporal evolution of species concentrations; it predicts average behaviors of large numbers of molecules. Both frameworks can handle spatial variability, e.g., by adopting operator splitting techniques for discrete reaction–diffusion processes (Choi et al. 2012) or partial-differential equations (PDEs) for their continuous counterparts.

Many systems involve reacting species with vastly different numbers of molecules/agents, thus necessitating the simultaneous use of discrete and continuous descriptors, i.e., call for the use of hybrid simulations. This occurs when a PDE-based model for one or more species fails to accurately capture salient features of a biological system either locally, in a (small) part of a computational domain (Bakarji and Tartakovsky 2017; Taverniers and Tartakovsky 2017), or globally, over the whole simulation domain (Choi et al. 2010). These two types of hybrid simulations differ in the way they couple their discrete and continuous components. We focus on the latter class of phenomena, of which leukocyte migration towards a pathogen is a pertinent example. It is worth to mention that simulations to represent the collective behaviors of chemotaxis are well studied in different scales (Di Costanzo et al. 2019; Guo et al. 2008; Othmer and Hillen 2002). Moreover, hybrid models are widely used to connect different scales in many other biological processes, e.g., (Anderson and Chaplain 1998; Choi et al. 2012; Dallon and Othmer 1997, 2004; Deisboeck et al. 2011; Lowengrub et al. 2009; Ruiz-Martinez et al. 2019).

Leukocytes, or white blood cells, are instrumental in a body’s immune response to invading pathogens, such as bacteria, viruses, or parasites. A pathogen-induced inflammation activates leukocytes in the bloodstream, causing their transmigration from blood vessels to the surrounding tissue. Within the affected tissue, leukocytes move towards a contaminated site, exhibiting undirected (diffusion-like) and directed (chemotaxis) forms of motion as well as interacting with a pathogen. Continuum-level representations of the latter stage of leukocyte migration rely on systems of coupled PDEs of various degrees of complexity, ranging from the celebrated Keller-Segel chemotaxis model (Keller and Segel 1971) to its more evolved counterparts (Hillen and Painter 2009). Such models track concentrations of relevant species—the concentrations of leukocytes,  $\mathcal{L}(\mathbf{x}, t)$ , and chemoattractant,  $\mathcal{A}(\mathbf{x}, t)$ , in the Keller-Segel model (Keller and Segel 1971)—in space,  $\mathbf{x}$ , and time,  $t$ . While large numbers of

chemoattractant molecules justify the use of a PDE-based model to describe the spatiotemporal evolution of  $\mathcal{A}(\mathbf{x}, t)$ , relatively small numbers of leukocytes and bacteria involved in the process render such continuum treatments problematic. Taken in isolation, the motion of individual leukocytes has been described by, e.g., biased random walk (Alt 1980; Tranquillo and Lauffenburger 1990).

We present a hybrid algorithm that combines a continuum description of chemoattractants with discrete representations of leukocytes and bacteria. Section 2 provides a mathematical model of leukocyte migration towards an inflammation site, including its continuum (PDE-based) formulation. Our hybrid method and its algorithmic implementation are presented in Sect. 3. They are used in Sect. 4 to solve three problems of increasing complexity. The first, a one-dimensional advection-diffusion equation, serves to verify our algorithm by comparing its predictions with an analytical solution and to analyze the effect of a finite number of particles on the adequacy of the continuum model. The second, unidirectional leukocyte migration in the presence of chemoattractant and bacteria, accomplishes the same goals by comparing our predictions with those provided by solving numerically a system of one-dimensional chemotaxis–motility–reaction PDEs. The third problem deals with a more realistic two-dimensional setting, which represents leukocyte migration towards a wound. Main conclusions drawn from our study are summarized in Sect. 5.

## 2 Model of leukocyte migration

We consider a model that involves leukocytes (L), bacteria (B), and chemoattractant (A). Its continuum representation relies on their respective concentrations  $\mathcal{L}(\mathbf{x}, t)$ ,  $\mathcal{B}(\mathbf{x}, t)$  and  $\mathcal{A}(\mathbf{x}, t)$ . The speed with which these three species diffuse through a tissue is characterized by a diffusion coefficient of the chemoattractant,  $D$ , and motility coefficients of leukocytes,  $\mu_L$ , and bacteria,  $\mu_B$ . Leukocytes are also advected with a chemotactic velocity  $\mathbf{V}_{\text{ch}} = (V_1, V_2)^\top$ , which depends on both the chemoattractant concentration  $\mathcal{A}$  and its gradient  $\nabla\mathcal{A}$ . The  $i$ th component of this velocity vector is given by Zigmond (1977, 1981)

$$V_i = v_i \frac{u_i}{1 + u_i} \text{sign} \left( \frac{\partial \mathcal{A}}{\partial x_i} \right), \quad u_i = \chi_0 \frac{\partial N_{\text{br}}}{\partial \mathcal{A}} \left| \frac{\partial \mathcal{A}}{\partial x_i} \right|; \quad (1)$$

where  $v_i$  with  $i = 1, 2$  are the maximum velocities of a leukocyte in the  $i$ th direction;  $\chi_0$  is chemotactic sensitivity; and  $N_{\text{br}}$  is the number of bound receptors on the cell membrane. The latter is related to the concentration of chemoattractant  $\mathcal{A}$  by the Michaelis-Menten relationship

$$N_{\text{br}} = \frac{N_{\text{tot}} \mathcal{A}}{K_d + \mathcal{A}}, \quad (2)$$

where  $N_{\text{tot}}$  is the total number of cell receptors on the cell membrane, and  $K_d$  is the receptor dissociation constant. The term  $\phi = u_i / (1 + u_i)$  is referred to as orientation bias.

Finally, the three species involved undergo biological transformations. Chemoattractant A is released from the bacteria B at the wound site with production rate  $k_p$ ,



Bacteria B are reproduced with growth rate  $k_g$ ,



leukocytes L die with natural death rate  $g_0$ ,



and, upon encountering each other, a leukocyte and a bacterium die at the same rate  $g_1$ ,



The latter reaction needs no activation energy; it is reaction-dominated and takes place when a leukocyte of effective radius  $r_L$  and a bacterium of effective radius  $r_B$  touch, with reaction rate constant  $g_1$  determined by their motility rates,

$$k_d = 4\pi(r_B + r_L)(\mu_B + \mu_L) \cdot N_{Av} \cdot 10^{-3} [\text{M}^{-1} \cdot \text{s}^{-1}], \quad (4)$$

where  $N_{Av}$  is the Avogadro number.

The overall chemotaxis–motility–reaction system is described by a system of PDEs

$$\frac{\partial \mathcal{A}}{\partial t} = D \nabla^2 \mathcal{A} + k_p \mathcal{B}, \quad (5a)$$

$$\frac{\partial \mathcal{L}}{\partial t} = -\nabla \cdot \mathbf{J}_c - (g_0 + g_1 \mathcal{B}) \mathcal{L}, \quad (5b)$$

$$\frac{\partial \mathcal{B}}{\partial t} = \mu_B \nabla^2 \mathcal{B} + (k_g - k_d \mathcal{L}) \mathcal{B}, \quad (5c)$$

with  $\mathbf{J}_c = -\mu_L \nabla \mathcal{L} + \mathbf{V}_{ch}(\mathcal{A}, \Delta \mathcal{A}) \mathcal{L}$ . Biological processes represented by this model of immune response are depicted in Fig. 1.

Numerical solution of this system, obtained with the second-order TVD scheme (LeVeque 2002) for chemotaxis and Newton-Raphson iterations for reactions, serves as a continuum-level model.

### 3 Materials and methods

Standard numerical methods for solving (5), e.g., finite elements and finite volume schemes, often falter when deployed to model chemotaxis and diffusion phenom-

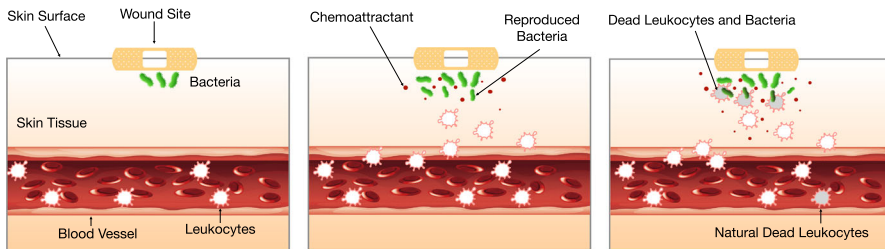


**Fig. 1** The stages of immune response to inflammation represented in our model. Left: The initial stage of inflammation. Middle: Reproduction of bacteria and release of chemoattractants by bacteria, which triggers leukocytes migration. Right: Leukocytes die either naturally or upon encountering bacteria

ena over long simulation time (Tyson et al. 2000; Ward et al. 2011; Bosma et al. 1988). The vastly different time scales between the biochemical reactions and the transport processes render the system of PDEs (5) rather stiff, further complicating its numerical treatment. Methods for dealing with stiffness include operator splitting (Strang 1968), which uses an explicit scheme to handle chemotaxis and motility, and an implicit method to deal with the (stiff) reactions. The computationally intensive Newton-Raphson method is usually employed to treat the reactions between the bacteria ( $B$ ) and leukocytes ( $L$ ) implicitly. These numerical strategies do not address the foundational limitation of deterministic PDE-based models of leukocyte migration, such as (5): relatively small numbers of leukocytes and bacteria undermine the validity of their continuum-level descriptions.

Our hybrid model comprises continuum and discrete modules, which explicitly account for the vast disparity in the number of chemoattractant molecules on one hand and the number of leukocytes and bacteria on the other. In a chemotaxis–motility–reaction system, chemoattractant is adequately represented by its concentration  $\mathcal{A}$ , and its diffusion and production are captured by (5a). Relatively small populations of bacteria and leukocytes are described by discrete stochastic analogues of (5b) and (5c). These processes, and their descriptors, are coupled because, in each element of a numerical mesh, the concentration of chemoattractant  $\mathcal{A}$  is affected by the local number of bacteria  $N_B$ , and the chemotactic drift velocity of leukocytes  $\mathbf{V}_{ch}$  is determined by the local value of  $\mathcal{A}$  (and its gradient). Random positions of individual bacteria and leukocytes are determined by their motility and, in the case of leukocytes, by the chemotactic velocity  $\mathbf{V}_{ch}$ . Bacteria and leukocytes annihilate each other when they come into close contact.

### 3.1 Continuum module: chemoattractant

Chemoattractant  $A$  is produced by bacteria  $B$  and is spread by diffusion. In the early stage of inflammation, the chemoattractant concentration  $\mathcal{A}(\mathbf{x}, t)$  is much higher than the concentrations (local numbers) of bacteria and leukocytes. For this reason, we use (5a) to describe its spatiotemporal evolution. Using two-dimensional simulations as an example, a computational domain is discretized by a uniform mesh, which

consists of  $N_x \times N_y$  elements with uniform mesh size  $\Delta x \times \Delta y$ . Numerical solution of (5a) relies on an implicit-explicit (IMEX) finite volume scheme. For  $\mathbf{x} = (x, y)^\top$  and  $\mathcal{A}_{i,j}^n \equiv \mathcal{A}(i \Delta x, j \Delta y, n \Delta t)$  with  $i = 1, \dots, N_x$  and  $j = 1, \dots, N_y$ , this yields, for the  $(n + 1)$ st time step,

$$\begin{aligned} \frac{\mathcal{A}_{i,j}^{n+1} - \mathcal{A}_{i,j}^n}{\Delta t} &= D \frac{\mathcal{A}_{i+1,j}^{n+1} - 2\mathcal{A}_{i,j}^{n+1} - \mathcal{A}_{i-1,j}^{n+1}}{\Delta x^2} \\ &+ D \frac{\mathcal{A}_{i,j+1}^{n+1} - 2\mathcal{A}_{i,j}^{n+1} - \mathcal{A}_{i,j-1}^{n+1}}{\Delta y^2} + k_p b_{i,j}^n. \end{aligned} \tag{6}$$

Defining  $s_x = D\Delta t/(\Delta x)^2$  and  $s_y = D\Delta t/(\Delta y)^2$ , this translates into

$$\begin{aligned} -s_y \mathcal{A}_{i,j-1}^{n+1} - s_x \mathcal{A}_{i-1,j}^{n+1} + (1 + 2s_x + 2s_y) \mathcal{A}_{i,j}^{n+1} \\ - s_x \mathcal{A}_{i+1,j}^{n+1} - s_y \mathcal{A}_{i,j+1}^{n+1} = \Delta t \mathcal{A}_{i,j}^n + \Delta t k_p b_{i,j}^n. \end{aligned} \tag{7}$$

The time-step size  $\Delta t$  is updated at every iteration, as explained in Sect. 3.3. This discretization produces a penta-diagonal matrix, whose inversion is well suited for the restarted Generalized Minimum Residual (GMRES) algorithm (Saad and Schultz 1986). If the continuum-level description of bacteria were valid, then  $b_{i,j}^n \equiv \mathcal{B}_{i,j}^n$ . Otherwise, it has to be replaced with its discrete (and stochastic) counterpart, as discussed in the section below.

Once  $\mathcal{A}$  at a given times step is computed, the chemotaxis velocity  $\mathbf{V}_{ch}$  is determined from (1) via automatic differentiation.

### 3.2 Discrete module: leukocytes and bacteria

Since transport (motility and/or chemotactic drift) and reactions take place at different time scales, we use stochastic operator splitting (Choi et al. 2012; Ruiz-Martinez et al. 2019). Motility (diffusion) of bacteria and motility and chemotaxis (advection-diffusion) of leukocytes are modeled via Brownian motion and Brownian motion with a drift, respectively. Chemical and/or biological transformations of bacteria and leukocytes within individual elements of the mesh are described via a (modified) Gillespie algorithm.

#### 3.2.1 Stochastic operator splitting

If the continuum model (5) were valid, then, during a time interval  $[t, t + \Delta t]$ , the operator splitting algorithm (Hundsdorfer and Verwer 2013) would replace (5b) and (5c) with

$$\frac{\partial \mathcal{L}'}{\partial t} = \mu_L \nabla^2 \mathcal{L}' - \nabla \cdot (\mathbf{V}_{ch} \mathcal{L}'), \tag{8a}$$

$$\frac{\partial \mathcal{B}'}{\partial t} = \mu_B \nabla^2 \mathcal{B}'. \tag{8b}$$

and

$$\frac{\partial \mathcal{L}''}{\partial t} = -(g_0 + g_1 \mathcal{B}'') \mathcal{L}'', \tag{9a}$$

$$\frac{\partial \mathcal{B}''}{\partial t} = (k_g - k_d \mathcal{L}'') \mathcal{B}''. \tag{9b}$$

Here  $\mathcal{L}'(t) = \mathcal{L}(t)$  and  $\mathcal{B}'(t) = \mathcal{B}(t)$ ; and  $\mathcal{L}''(t) = \mathcal{L}'(t + \Delta t)$  and  $\mathcal{B}''(t) = \mathcal{B}'(t + \Delta t)$ , so that  $\mathcal{L}''(t) = \mathcal{L}(t + \Delta t)$  and  $\mathcal{B}''(t) = \mathcal{B}(t + \Delta t)$ . Then, one would solve (8) and (9) on a fixed mesh with explicit and implicit methods, respectively.

Instead, we use meshless particle methods and stochastic simulations in the discrete setting. A discrete representation replaces the concentrations  $\mathcal{L}(\mathbf{x}, t)$  and  $\mathcal{B}(\mathbf{x}, t)$  at point  $\mathbf{x}$  with the numbers of leukocytes,  $N_L(\mathcal{V}_\mathbf{x}, t)$ , and bacteria,  $N_B(\mathcal{V}_\mathbf{x}, t)$ , in a volume  $\mathcal{V}_\mathbf{x}$  centered around point  $\mathbf{x}$ . We denote the position of the  $k$ th leukocyte and  $m$ th bacterium at time  $t$  by  $\mathbf{X}^{Lk}(t) = (X_1^{Lk}, X_2^{Lk})^\top$  and  $\mathbf{X}^{Bm}(t) = (X_1^{Bm}, X_2^{Bm})^\top$ , respectively.

### 3.2.2 Random motility and chemotaxis

We adapt the common assumption (Farrell et al. 1990) that the motility coefficients of populations of bacteria or leukocytes,  $\mu_B$  and  $\mu_L$ , coincide with those characterizing random motion of single bacterium and leukocyte. For leukocytes, this coefficient is calculated as

$$\mu_L = \frac{1}{2} T_p v^2, \tag{10}$$

where  $T_p$  is the persistence time (i.e., the time period between direction change); and, for the sake of simplicity and without loss of generality, we set the leukocyte maximum velocity in the  $i$ th direction to  $v_1 = v_2 = v$ . For bacteria, the motility coefficient  $\mu_B$  is relatively small; its experimentally determined value is listed in Table 1, together with values of the other parameters used in our model. The initial bacterial concentration is assumed to be the same as the initial leukocyte concentration.

Motion of bacteria and leukocytes are modeled as random walks with motility (Chandrasekhar 1943),

$$\mathbf{X}^{Lk}(t + \Delta t) = \mathbf{X}^{Lk}(t) + \mathbf{V}_{ch} \Delta t + \sqrt{2\mu_L \Delta t} \boldsymbol{\xi}, \tag{11a}$$

where  $k = 1, \dots, M_L$ ; and

$$\mathbf{X}^{Bm}(t + \Delta t) = \mathbf{X}^{Bm}(t) + \sqrt{2\mu_B \Delta t} \boldsymbol{\xi}, \tag{11b}$$

where  $m = 1, \dots, M_B$ . Here  $\boldsymbol{\xi}$  is a standard Gaussian random variable with the same dimension as  $\mathbf{X}^{Lk}$ ; and  $M_L$  and  $M_B$  are the total numbers of leukocytes and bacteria in the simulation, respectively.

**Table 1** Model parameters and their values used in numerical experiments

| Parameter        | Description                           | Value                             | References           |
|------------------|---------------------------------------|-----------------------------------|----------------------|
| $T_p$            | Persistence time                      | 300 s                             | Rivero et al. (1989) |
| $v$              | Max chemotactic velocity              | $2 \times 10^{-7}$ m              | Hoang et al. (2013)  |
| $\chi_0$         | Chemotactic sensitivity               | $4 \times 10^{-8}$ m/receptor     | Rivero et al. (1989) |
| $N_{\text{tot}}$ | Total receptors on cell membrane      | $5 \times 10^{10}$                | Rivero et al. (1989) |
| $K_d$            | Receptor dissociation constant        | $2 \times 10^{-8}$ s $^{-1}$      | Rivero et al. (1989) |
| $D$              | Diffusion coeff of chemoattractant    | $10^{-10}$ m $^2$ s $^{-1}$       | Rivero et al. (1989) |
| $\mu_L$          | Motility coeff of leukocyte           | Equation (10)                     |                      |
| $\mu_B$          | Motility coeff of bacteria            | $10^{-14}$ m $^2$ s $^{-1}$       | Rivero et al. (1989) |
| $r_B$            | Radius of bacteria                    | $10^{-6}$ m                       | Rivero et al. (1989) |
| $r_L$            | Radius of leukocyte                   | $1.4 \times 10^{-5}$ m            | Rivero et al. (1989) |
| $N_{\text{av}}$  | Avogadro number                       | $6.02 \times 10^{23}$ mol $^{-1}$ |                      |
| $k_p$            | Production rate of bacteria           | $10^{-6}$ s $^{-1}$               | Rivero et al. (1989) |
| $k_g$            | Generation rate of bacteria           | $3.47 \times 10^{-6}$ s $^{-1}$   | Su et al. (2009)     |
| $g_0$            | Decay rate of leukocyte               | $1.61 \times 10^{-5}$ s $^{-1}$   | Su et al. (2009)     |
| $k_d = g_1$      | Reaction rate of bacteria/leukocyte   | Equation (4)                      |                      |
| $\mathcal{A}_0$  | Initial chemoattractant concentration | $10^{-5}$ M                       | Walker et al. (1990) |
| $\mathcal{L}_0$  | Initial leukocyte concentration       | $8.3 \times 10^{-15}$ M           | Su et al. (2009)     |
| $\mathcal{B}_0$  | Initial bacterial concentration       | $8.3 \times 10^{-15}$ M           |                      |

### 3.2.3 Reactions

Within the  $(i, j)$  mesh element (for any  $i = 1, \dots, N_x$  and  $j = 1, \dots, N_y$ , as specified in Sect. 3.1), the bacteria and leukocytes are assumed to be well-mixed, so that Gillespie multi-particle (GMP) method (Rodríguez et al. 2006) can be used for particle-based treatment of chemical reactions and biological transformations. Let

$$n_L^{(i,j)}(t) = N_L(\mathcal{V}_{(x_i,y_j)}, t), \quad (12a)$$

$$n_B^{(i,j)}(t) = N_B(\mathcal{V}_{(x_i,y_j)}, t) \quad (12b)$$

denote the numbers of leukocytes and bacteria within the  $(i, j)$  mesh element, respectively. Then, the state of the system within that mesh element at any time  $t$  is described by the vector

$$\mathbf{n}^{(i,j)}(t) = (n_L^{(i,j)}, n_B^{(i,j)})^\top. \quad (13)$$

In GMP, the system is advanced from its current state at time  $t$  to its state at the (random) time  $t + \tau^{(i,j)}$ , with  $\tau^{(i,j)} < \Delta t$  for all  $i$  and  $j$ , by the following procedure.



First, one generates a random number  $r_1$  distributed uniformly on the unit interval  $[0, 1]$ . Second, the size of the reaction time step  $\tau^{(i,j)}$  is selected probabilistically as

$$\tau^{(i,j)} = -\frac{\ln r_1}{a_{\text{sum}}^{(i,j)}}, \tag{14}$$

where  $a_{\text{sum}}^{(i,j)}$  is the sum of all propensity functions  $a_r^{(i,j)}$  in the mesh element  $(i, j)$ . The details on calculation of these propensity functions and GMP in general are provided in ‘‘Appendix A’’. After one reaction time step  $\tau^{(i,j)}$ , the system state  $\mathbf{n}^{(i,j)}(t)$  is updated by

$$\mathbf{n}^{(i,j)}(t + \tau^{(i,j)}) = \mathbf{n}^{(i,j)}(t) + \mathbf{v}^{(i,j)}, \tag{15}$$

where  $\mathbf{v}^{(i,j)} = (\Delta n_{\text{L}}^{(i,j)}, \Delta n_{\text{B}}^{(i,j)})^T$  is the change in the number of leukocytes and bacteria due to these reactions.

### 3.3 Time-step selection

A proper time step is determined by accounting for the time scales of chemotaxis, random motility, and reactions of leukocytes and bacteria. Leukocyte migration due to random motility and chemotaxis introduces a time constraint, which is expressed in terms of the Péclet number

$$\begin{aligned} \text{Pe} &= \frac{|\mathbf{V}_{\text{ch}}| h_{\text{min}}}{\mu_{\text{L}}} = \frac{\tau_{\text{motL}}}{\tau_{\text{ch}}}, \\ \tau_{\text{motL}} &= \frac{h_{\text{min}}^2}{2\mu_{\text{L}}d}, \quad \tau_{\text{ch}} = \frac{h_{\text{min}}}{|\mathbf{V}_{\text{ch}}|}, \end{aligned} \tag{16}$$

where  $h_{\text{min}}$  is the smallest element-mesh size;  $d$  is a characteristic length scale; and  $\tau_{\text{motL}}$  and  $\tau_{\text{ch}}$  are the time scales of random motility and chemotaxis, respectively. The system in the  $(i, j)$  mesh element is diffusion-dominated if  $\text{Pe} < 1$  and advection-dominated if  $\text{Pe} > 1$ . We define the leukocyte migration time step as

$$\tau_{\text{mig}} = \min\{\tau_{\text{motL}}, \tau_{\text{ch}}\}. \tag{17}$$

By the same token, the time scale of bacterial random motility is  $\tau_{\text{motB}} = h_{\text{min}}^2/(2\mu_{\text{B}}d)$ . Since bacterium’s motility is much smaller than leukocyte’s, i.e., since  $\mu_{\text{B}} \ll \mu_{\text{L}}$ , the respective time scales satisfy the inequality  $\tau_{\text{motB}} \gg \tau_{\text{motL}}$ . Therefore, it is sufficient to consider  $\tau_{\text{motL}}$  when calculating the migration time step.

The reaction time step,  $\tau_{\text{reac}}$ , is chosen to be the smallest among the reaction time steps,  $t^{(i,j)}$ , for each mesh element  $(i, j)$ ,

$$\tau_{\text{reac}} \equiv \min\{t^{(i,j)} : i = 1, \dots, N_x; j = 1, \dots, N_y\}. \tag{18}$$

We define  $t^{(i,j)}$  as the upper bound of  $\tau^{(i,j)}$  in (14), i.e., set  $t^{(i,j)} = 1/a_{\text{sum}}^{(i,j)}$ . With the migration and reaction time scales thus defined, the system is characterized by the Damköhler number

$$\text{Da} = \frac{\tau_{\text{mig}}}{\tau_{\text{reac}}}. \quad (19)$$

At each time step in the simulation, the system is migration-dominated if  $\text{Da} > 1$  or reaction-dominated if  $\text{Da} < 1$ . In the reaction-dominated regime, the system is well mixed and is advanced by the migration time step,  $\Delta t = \tau_{\text{mig}}$ . In the migration-dominated regime,  $\Delta t$  should be larger than  $\tau_{\text{reac}}$  in order to provide enough time for the reaction between a bacterium and a leukocyte to take place (Choi et al. 2012). In summary, we set

$$\Delta t = \begin{cases} \tau_{\text{mig}} & \text{if } \text{Da} < 1, \\ 5\tau_{\text{mig}} & \text{if } 0.5 < \text{Da} < 1.0, \\ 10\tau_{\text{mig}} & \text{if } \text{Da} < 0.5. \end{cases} \quad (20)$$

Note that  $\Delta t$  is recomputed at each simulation step; and other strategies for the time-step selection are available (Ruiz-Martinez et al. 2019).

### 3.4 Algorithm

A detailed algorithm for hybrid simulations of the inflammation process during time interval  $[t_0, T]$  is summarized below.

1. Initialize  $t = t_0$
2. While  $t \leq T$ 
  - (a) Determine whether the system is migration- or reaction-dominated
    - i. Calculate  $\text{Pe}$  from (16);  $\tau_{\text{mig}}$  from (17);  $\tau_{\text{reac}}$  from (18); and  $\text{Da}$  from (19)
    - ii. Determine  $\Delta t$  from (20)
  - (b) Set  $t_{\text{old}} = t$
  - (c) Perform the migration and reaction steps using the operator-splitting method
    - i. Migration with time step  $\Delta t$ 
      - Find  $\mathcal{A}$  from (7)
      - Calculate  $\mathbf{V}_{\text{ch}}$  from (1)
      - Assign  $\mathbf{V}_{\text{ch}}$  to each leukocyte based on its current position  $\mathbf{X}^{\text{L}k}$
      - Use (11) to update positions of all leukocyte and bacteria  $\mathbf{X}^{\text{L}k}$  and  $\mathbf{X}^{\text{B}m}$
    - ii. Reactions within each mesh element  $(i, j)$ 
      - Count the numbers of leukocyte and bacteria,  $\mathbf{n}^{(i,j)}$  in (13), from the distributions of  $\mathbf{X}^{\text{L}k}$  and  $\mathbf{X}^{\text{B}m}$
      - while  $(t - t_{\text{old}}) \leq \Delta t$ 
        - Calculate  $\tau^{(i,j)}$  from (14)
        - If  $\tau^{(i,j)} \leq \Delta t$ , use (15) to update  $\mathbf{n}^{(i,j)}$

- Otherwise, do not update  $\mathbf{n}^{(i,j)}$   
 end *while*  
 - Go to the next mesh element; repeat  
 (d)  $t = t_{\text{old}} + \Delta t$   
 end *while*

### 3.5 Initial and boundary conditions

In our simulations of the inflammation caused by a wound at time  $t_0$ , leukocytes migrate from a capillary/venule with surface  $\Gamma_{\text{cap}}$  towards bacteria in the wound at the skin surface  $\Gamma_{\text{sk}}$ . We model this process by placing, at time  $t = 0$ , leukocytes and bacteria along small segments of these surfaces. This gives rise to the initial conditions

$$\begin{aligned} \mathcal{L}(\mathbf{x}, t_0) &= \mathcal{L}_0(\mathbf{x}), \quad \mathbf{x} \in \Gamma_{\text{cap}} \\ \mathcal{B}(\mathbf{x}, t_0) &= \mathcal{B}_0(\mathbf{x}), \quad \mathbf{x} \in \Gamma_{\text{sk}}, \end{aligned} \tag{21}$$

or their discrete counterpart

$$\begin{aligned} N_L(\mathcal{V}_{\mathbf{x}}, t_0) &= N_{L_0}(\mathcal{V}_{\mathbf{x}}), \quad \mathbf{x} \in \Gamma_{\text{cap}} \\ N_B(\mathcal{V}_{\mathbf{x}}, t_0) &= N_{B_0}(\mathcal{V}_{\mathbf{x}}), \quad \mathbf{x} \in \Gamma_{\text{sk}}. \end{aligned} \tag{22}$$

In either case, the initial concentration of the chemoattractant is  $\mathcal{A}(\mathbf{x}, t_0) = 0$  for  $\mathbf{x} \in \Omega$ . If leukocytes leave the capillary at point  $\mathbf{x}_{\text{cap}} \in \Gamma_{\text{cap}}$  and bacteria enter the tissue at point  $\mathbf{x}_{\text{sk}} \in \Gamma_{\text{sk}}$ , then the initial concentrations  $\mathcal{L}_0$  and  $\mathcal{B}_0$ , or their discrete counterparts  $N_{L_0}(\mathcal{V}_{\mathbf{x}})$  and  $N_{B_0}(\mathcal{V}_{\mathbf{x}})$ , are non-zero only in the mesh element containing  $\mathbf{x}_{\text{cap}}/\mathbf{x}_{\text{sk}}$ .

Our choice of boundary conditions is motivated by the one-dimensional study of Lauffenburger and Keller (1979). The scenario in which leukocytes and bacteria, once in the tissue, cannot leave it through the blood vessel and the skin is modeled by treating  $\Gamma_{\text{cap}}$  and  $\Gamma_{\text{sk}}$  as impermeable surfaces. This gives rise to the boundary conditions

$$\mathbf{n} \cdot (\mu_L \nabla \mathcal{L} - \mathbf{V}_{\text{ch}} \mathcal{L}) = 0, \quad \mathbf{n} \cdot \nabla \mathcal{B} = 0, \quad \mathbf{x} \in \Gamma_{\text{cap}} \cup \Gamma_{\text{sk}}. \tag{23}$$

In the particle simulations, the reflective boundary conditions are imposed along  $\Gamma_{\text{cap}}$  and  $\Gamma_{\text{sk}}$ . During the modeling process, the chemoattractant concentration at the wound site (e.g., the point  $\mathbf{x}_{\text{sk}} \in \Gamma_{\text{sk}}$ ) remains constant,  $\mathcal{A}_0$ , once the inflammation process starts. The remainder of the skin is impervious to chemoattractant diffusion. Hence,

$$\mathcal{A}(\mathbf{x}_{\text{sk}}, t) = \mathcal{A}_0, \quad \mathbf{n} \cdot \nabla \mathcal{A} = 0, \quad \mathbf{x} \in \Gamma_{\text{sk}}/\{\mathbf{x}_{\text{sk}}\}. \tag{24a}$$

It is common to assume (Lauffenburger and Keller 1979) that the chemoattractant moves between the bloodstream and tissue across the venule wall  $\Gamma_{\text{cap}}$ . The rate of net

movement across the wall is postulated to be proportional to the difference between the concentrations at the two sides of the wall, with a constant of proportionality (transfer coefficient)  $h_a$  quantifying the ease of movement across the wall:

$$D \mathbf{n} \cdot \nabla \mathcal{A} = h_a (\mathcal{A}_{\text{cap}} - \mathcal{A}), \quad \mathbf{x} \in \Gamma_{\text{cap}}. \quad (24b)$$

In the simulations reported below, we set the chemoattractant concentration in the venule wall to  $\mathcal{A}_{\text{cap}} = 0$ .

We use these boundary conditions for the sake of concreteness and to demonstrate the capabilities of our hybrid algorithm. They can be replaced with other boundary conditions, e.g., those used in Beesley et al. (1978) or Fehr and Jacob (1977), in order to account for transient circulatory leukocyte mobilization, diffusion of chemoattractant through the wall, etc. We leave these and other model enhancements for future studies.

## 4 Numerical experiments

We conduct several numerical experiments to demonstrate the accuracy of our hybrid method and its ability to predict salient stochastic features of leukocyte chemotaxis during inflammation. The first test, reported in “Appendix B.1”, illustrates the close agreement between the solution of a PDE and its discrete counterpart when the number of particles used in the latter is large.

The same conclusion is reached in the second test, which deals with the one-dimensional version of the chemotaxis–motility–reaction system (5) for small, intermediate, and large populations of leukocytes and bacteria (“Appendix B.2”). Strong stochastic effects are observed for small populations, while large numbers result in predictions consistent with the numerical solution of (5).

This one-dimensional setting has been the subject of previous theoretical studies that established bacteria elimination criterion for steady-state (Lauffenburger and Keller 1979) and transient (Alt and Lauffenburger 1987) chemoattractant concentrations. In both regimes, the criterion identifies four culprits of infection: (i) low numbers of circulating leukocytes; (ii) defective phagocytosis or toxic bacteria; (iii) short-lived leukocytes; and (iv) large tissue radius  $R$ . While our model is considerably more evolved than the original models (Lauffenburger and Keller 1979; Alt and Lauffenburger 1987), our stochastic/hybrid simulations account for each of these factors by modifying the baseline state with  $N_{B_0} = 8000$  and  $N_{L_0} = 10,000$  (Fig. 2) as follows: (i) decrease the number of leukocytes to  $N_{L_0} = 80$ ; (ii) decrease the reaction rate  $k_d$  by  $10^{20}$ ; (iii) increase leukocyte natural death rate  $g_0$  by 100; and (iv) increase the size of the simulation domain to  $R = 10^{-2}$  m. Figure 2 shows that any of these four deficiencies indeed can trigger an infection, i.e., cause leukocytes to die out in a finite time and bacteria to survive and multiply.

The third test deals with two-dimensional models, in which stochastic simulations are conducted in a domain with multiple entrances for leukocytes from a blood vessel (Fig. 3). The simulation domain  $\Omega$  is a rectangle  $[x_{\text{in}}, x_{\text{out}}] \times [y_{\text{sk}}, y_{\text{cap}}]$ , such that the skin is located at  $y = y_{\text{sk}} = 0$ , the blood vessel at  $y = y_{\text{cap}}$ , and  $R = y_{\text{cap}} - y_{\text{sk}}$  denotes the tissue radius in the Krogh model (Krogh 1922). The length of the blood

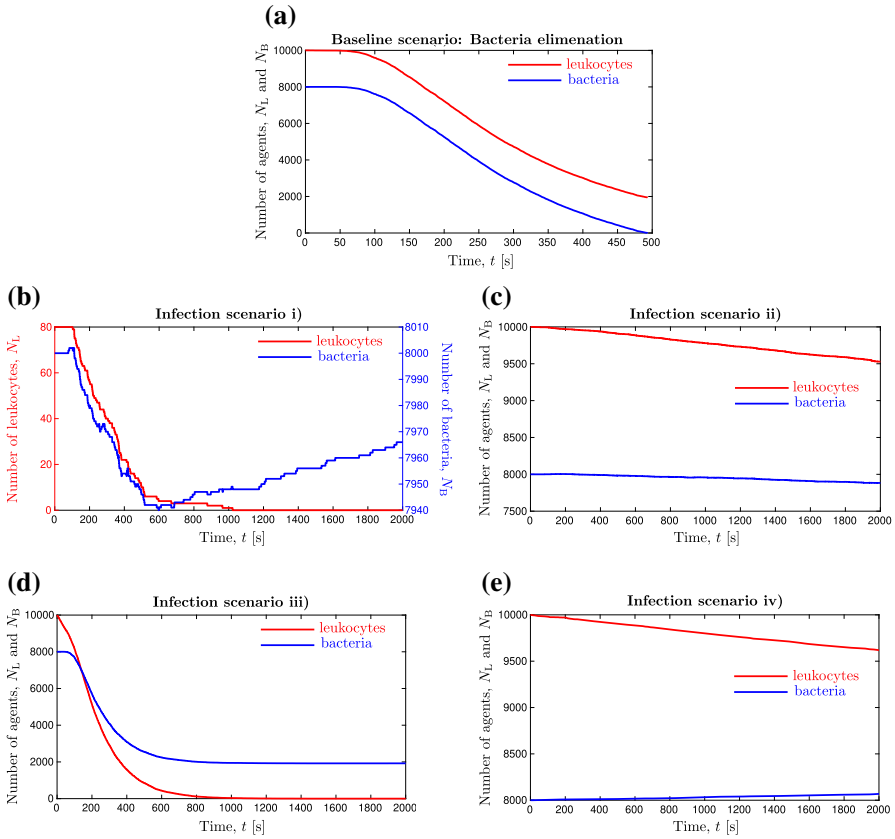
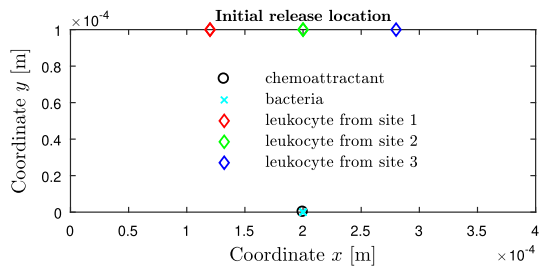


**Fig. 2** Change in the number of leukocytes and bacteria in **a** the baseline scenario with  $N_{L0} = 10,000$  and  $N_{B0} = 8,000$ ; and scenarios with **b** the number of leukocytes decreased to  $N_{L0} = 80$ , **c**  $k_d$  decreased by  $10^{20}$ , **d**  $g_0$  increased by 100, and **e** the domain size increased by 10

**Fig. 3** Two-dimensional simulation domain. The skin is located at  $y = y_{sk} = 0$ , and the capillary at  $y = y_{cap} = 10^{-4}$  m



vessel and the simulation domain is  $L_x = x_{out} - x_{in}$ . The wound is located at  $\mathbf{x}_{sk} = (L_x/2, y_{sk} = 0)^T$ , as is initially bacteria.

Once the chemoattractant is released at  $t = t_0 = 0$ , leukocytes transmigrate from the blood, through the endothelial layer of the capillary, to the wound site during the inflammation process. We allow for this process to occur at three sites along the

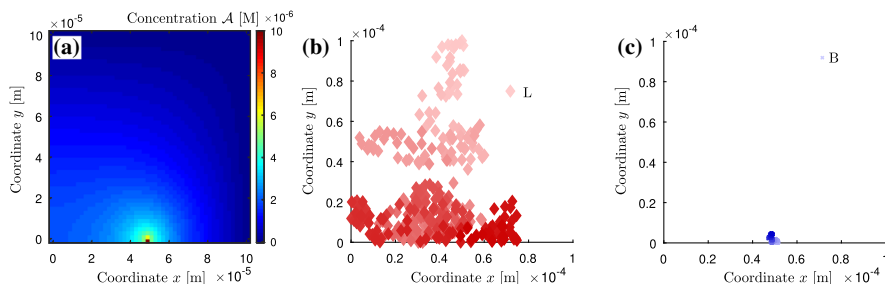
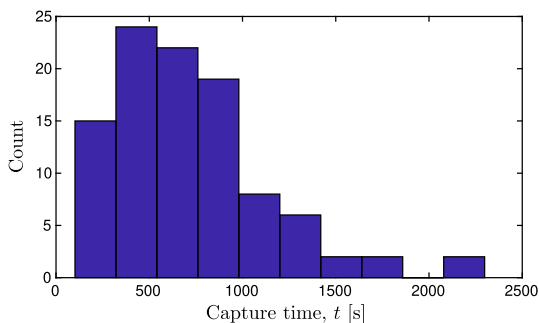


**Fig. 4** A leukocyte chasing a bacterium in the tissue: **a** chemoattractant concentration  $\mathcal{A}$  at the capture time  $t = 533.333$  s, **b** trajectory of the leukocyte; and **c** trajectory of the bacterium. Lighter shades represent positions at earlier times and darker color represent positions at later times. Big red diamonds are leukocyte traces, and small blue crosses are bacteria traces

**Fig. 5** Histogram of the capture time of the bacterium by the leukocyte from 100 simulations



capillary:  $x_{L_1} = 0.3L_x$ ,  $x_{L_2} = 0.5L_x$ , and  $x_{L_3} = 0.7L_x$  (Fig. 3). The release is assumed to occur at specified number of particles  $N_{L_1}$ ,  $N_{L_2}$ , and  $N_{L_3}$ , respectively, in accordance with (22).

### 4.1 One leukocyte chasing one bacterium

A leukocyte is released at  $x_{\text{cap}} = L_x/2$ , i.e., we set  $N_{L_1} = 0$ ,  $N_{L_2} = 1$ , and  $N_{L_3} = 0$ . The simulation domain size is  $L_x = 10^{-4}$  m and  $R = 10^{-4}$  m, and the chemoattractant’s diffusion coefficient is  $D = 10^{-12}$  m<sup>2</sup>s<sup>-1</sup>. All other parameters have the values specified in Table 1.

This setup mimics the 16 mm movie made by D. Rogers in the 1950s (Rogers xxxx). Figure 4 exhibits the chemoattractant concentration and trajectories of the leukocyte and bacterium. The bacterium diffuses in the vicinity of the wound because of its small motility. The leukocyte has more freedom to explore the space, covering much of the  $10^{-4}$  m by  $10^{-4}$  m square area of the tissue. Figure 5 shows the histogram of the capture time of the bacterium by the leukocyte from 100 simulations, with an average of 711.3 s.

Results of similar simulations for small ( $N_{L_0} = N_{B_0} = 5$ ) and large ( $N_{L_0} = N_{B_0} = 8 \times 10^5$ ) populations of leukocytes and bacteria are presented in “Appendix B.3”. As expected, the former setting gives rise to appreciable stochastic fluctuations, which

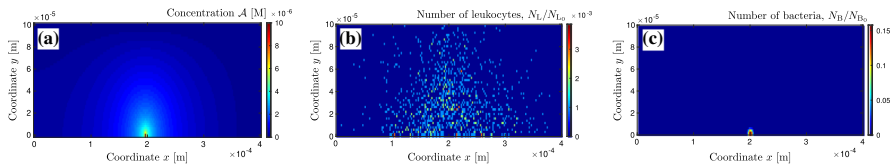


**Fig. 6** Intermediate-size populations of leukocytes and bacteria. Temporal snapshots, at time  $t = 1000$  s, of **a** the chemoattractant concentration and the numbers of **b** leukocytes and **c** bacteria, normalized with their initial population numbers

cannot be captured with the deterministic, PDE-based model (5). These fluctuations average out in the latter setting, so that the stochastic (hybrid) and deterministic (PDE-based) models yield similar predictions. Results for populations of intermediate size are presented below.

## 4.2 Intermediate populations of leukocytes and bacteria

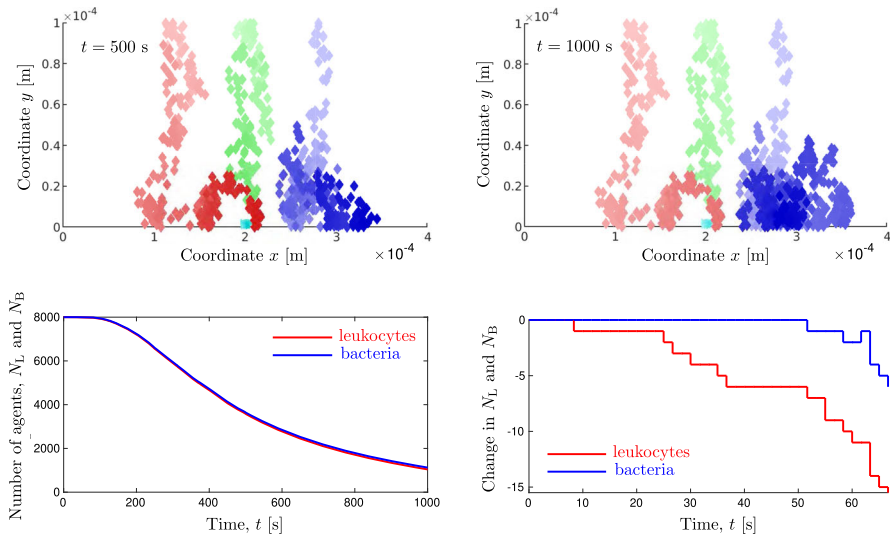
In this experiment, the total of  $N_{L_0} = 8000$  leukocytes enter the tissue at three sites:  $N_{L_1} = 3000$  at  $x_{L_1}$ ,  $N_{L_2} = 3000$  at  $x_{L_2}$ , and  $N_{L_3} = 2000$  at  $x_{L_3}$ . They attack  $N_{B_0} = 8000$  released at the wound (Fig. 3). Figure 6 exhibits a temporal snapshot (at  $t = 1000$  s) of the chemoattractant concentration and the numbers of leukocytes and bacteria, normalized respectively by  $N_{L_0}$  and  $N_{B_0}$ . By this time, the leukocytes have spread all over the tissue due to random walk with large motility, while the bacteria are concentrated near the wound due to their small motility. However, very few leukocytes exist near the wound because the leukocytes die after annihilating the invading bacteria during phagocytosis.

Figure 7 shows the trajectories of three leukocytes released from the blood vessel at the three sites. All of them exhibit the same pattern of Brownian motion and chemotaxis as those observed in small populations (“Appendix B.3”). The rate of decrease in the numbers of leukocytes and bacteria grows in the presence of large populations. The last frame in Fig. 7 zooms in on the early stage of the process, highlighting both the natural death of leukocytes and the growth of bacteria before their interactions take place.

Finally, we report the computational time for the simulation time horizon of 2000 s for 1D and 200 s for 2D using Intel(R) Core(TM) i7-6700 at 3.40 GHz processor. The mean CPU time and variance, calculated from twenty realizations, are reported in Table 2. The time step of the deterministic PDE solver is set to  $\min\{\Delta x^2/2D, \Delta x/|V_{ch}|\}$ , considering the Péclet number. The hybrid simulation is more efficient, accurate and informative for systems with small and intermediate population sizes ( $N_{L_0} = N_{B_0}$ ).

## 5 Summary and conclusions

Multiscale features of complex biological systems undermine the validity, and raise computational cost, of continuum (PDE-based) descriptors. We developed a hybrid



**Fig. 7** Intermediate-size populations of leukocytes and bacteria. Top row: trajectories of a few leukocytes and bacteria at  $t = 500$  s and  $t = 1000$  s. The lighter shades represent positions at earlier time, and darker shades represent positions at later times. Red diamonds represent the leukocytes released from  $x_{L1}$ , green diamonds from  $x_{L2}$ , and blue diamonds from  $x_{L3}$ ; cyan crosses designate a representative bacterium trace; Bottom row: the reduction in the numbers of leukocytes and bacteria versus time, and its magnified behavior during the early stage

**Table 2** Computational time for the deterministic PDE solver and hybrid simulations with different population sizes

|                       | Mean CPU time (min) | Variance |
|-----------------------|---------------------|----------|
| PDE solver            | 60.7083             | –        |
| Hybrid, $N_0 = 8$     | 33.1574             | 2.6404   |
| Hybrid, $N_0 = 80$    | 34.1768             | 1.0551   |
| Hybrid, $N_0 = 800$   | 37.1287             | 0.2009   |
| Hybrid, $N_0 = 8000$  | 41.7389             | 0.3618   |
| Hybrid, $N_0 = 80000$ | 65.9329             | 0.2449   |

Twenty realizations are conducted to compute the mean CPU time and variance

algorithm that combines continuum and stochastic methods to handle these challenges. Its general features and performance were demonstrated on a model of inflammation, which describes leukocyte migration towards, and phagocytosis of, bacteria invading the tissue from a skin wound.



The solution algorithm involves three inter-connected components. The first comprises a continuum (PDE-based) model of diffusion and reactions of chemoattractant. The second component deals with discrete (stochastic) simulations of the movement of individual leukocytes and bacteria in the tissue: motility of both is modeled via Brownian motion, with the drift due to chemotactic (chemoattractant-dependent) velocity added for the former. The third component consists of a discrete (stochastic) computation of biochemical transformations, which utilizes the modified Gillespie multi-particle method. In each mesh element and at each time step, the time step size is autonomously modified depending on whether the system is locally at a diffusion-advection- or reaction-dominated state, as measured by the local Péclet and Damköhler numbers.

For small and intermediate populations of leukocytes and bacteria, our hybrid method yields more accurate simulation results in much less computation time than the deterministic PDE-based solver. For large populations, the two methods yield similar results; the PDE-based solver is faster, but the hybrid method provides more informative individual properties on the fly.

Understanding the conditions under which infection persists helps identify both intrinsic deficiencies in the host system and superior features of invading bacteria. Deterministic models are of limited use in determining an elimination/infection time and examining the sensitivity to different biological parameters. That is because (at least one) species decreases to a small population at later stages of either elimination or infection. Our simulations demonstrate that concentrations, and deterministic PDE-based models, do not provide accurate descriptors of the dynamics of small populations. Given the presence of chemoattractant with relatively large concentrations, only a continuum-discrete hybrid model of the kind developed in this study can provide an accurate, yet computationally efficient, simulation tool in applications such as detecting immune system defects and monitoring antibiotic responses.

In summary, the proposed hybrid method is advantageous in multi-species biological and biochemical systems whose dynamic behavior is manifest on dramatically different time scales. It can be utilized as a powerful tool to simulate laboratory experiments and test infection diagnosis, among other applications.

**Acknowledgements** We thank the two anonymous reviewers and the Associate Editor for their insightful comments, which helped us to improve our manuscript.

**Data Availability** The data that support the findings of this study are available within the article.

## A GMP simulation

In each mesh element  $(i, j)$  at any time  $t$ , the system is described by the numbers of leukocytes and bacteria  $\mathbf{n}^{(i,j)}(t)$ , as defined in (12) and (13). The superscript  $(i, j)$  is omitted below to simplify the notation.

Let  $\mathbb{P}_0[\tau|\mathbf{n}, t]$  denote the (conditional) probability of no reactions taking place during the time interval  $[t, t + \tau]$  provided that the system is at state  $\mathbf{n}$  at time  $t$ . The reaction system is assumed to be Markovian, i.e., the probability that no reactions occur during  $[t, t + \tau + d\tau]$  equals the product of the probabilities of no reactions

**Table 3** Propensity functions for the leukocytes-bacteria-chemoattractant system

| Reaction                            | Number, $r$ | Propensity function, $a_r$ |
|-------------------------------------|-------------|----------------------------|
| $B \xrightarrow{k_g} 2B$            | 1           | $a_1 = k_g N_B$            |
| $L \xrightarrow{g_0} \emptyset$     | 2           | $a_2 = g_0 N_L$            |
| $B + L \xrightarrow{g_1} \emptyset$ | 3           | $a_3 = k_d N_B N_L$        |

occurring during  $[t, t + \tau)$  and during  $[t + \tau, t + \tau + d\tau)$ . A propensity function  $a_r$  is defined such that  $a_r d\tau$  is the probability that both the next reaction will be the  $r$ th reaction and it will occur during  $[t + \tau, t + \tau + d\tau]$ . Then, one obtains (Gillespie 1976)

$$\mathbb{P}_0[\tau + d\tau | \mathbf{n}, t] = \mathbb{P}_0[\tau | \mathbf{n}, t](1 - a_{\text{sum}}(\mathbf{n})d\tau),$$

$$a_{\text{sum}}(\mathbf{n}) = \sum_{r=1}^S a_r(\mathbf{n}), \tag{25}$$

where  $S$  is the number of chemical reactions. Taking the limit as  $d\tau \rightarrow 0$  and solving the resulting PDE leads to

$$\mathbb{P}_0(\tau | \mathbf{n}, t) = e^{-a_{\text{sum}}(\mathbf{n})\tau}. \tag{26}$$

The propensity functions for the reactions in (3) are listed in Table 3.

It follows from the definition of  $\mathbb{P}_0$  and  $a_r$  that the probability  $\mathbb{P}(\tau, r | \mathbf{n}, t)$  of both the next reaction being the  $r$ th reaction and occurring during  $[t + \tau, t + \tau + d\tau)$ , given the present state of the system  $\mathbf{n}(t)$ , is

$$\mathbb{P}(\tau, r | \mathbf{n}, t) = \mathbb{P}_0[\tau | \mathbf{n}, t] a_r(\mathbf{n}). \tag{27}$$

Accounting for (26),

$$\mathbb{P}(\tau, r | \mathbf{n}, t) = \frac{a_r(\mathbf{n})}{a_{\text{sum}}(\mathbf{n})} a_{\text{sum}}(\mathbf{n}) e^{-a_{\text{sum}}(\mathbf{n})\tau}. \tag{28}$$

The ratio  $a_r(\mathbf{n})/a_{\text{sum}}(\mathbf{n})$  represents the probability of a discrete random variable: the label of the next reaction. The term  $a_{\text{sum}}(\mathbf{n}) \exp[-a_{\text{sum}}(\mathbf{n})\tau]$  is the exponential density function of a continuous random variable: the time at which the next reaction will occur.

The GMP algorithm for reactions is presented below.

For  $i = 1, \dots, N_x$

For  $j = 1, \dots, N_y$

1. Count  $n_L^{(i,j)}$  and  $n_B^{(i,j)}$ , the numbers of leukocytes and bacteria in the mesh element  $(i, j)$
2. Generate random numbers  $r_1$  and  $r_2$  distributed uniformly on the interval  $[0, 1]$ ; use (14) to determine the reaction time step  $\tau^{(i,j)}$
3. If  $\tau^{(i,j)} \leq \Delta t$ 
  - if  $r_2 a_{\text{sum}}^{(i,j)} < a_1^{(i,j)}$ , reaction 1 happens:  $\mathbf{n}^{(i,j)}(t + \tau^{(i,j)}) = \mathbf{n}^{(i,j)}(t) + [0, 1]^T$
  - if  $a_1^{(i,j)} \leq r_2 a_{\text{sum}}^{(i,j)} < a_1^{(i,j)} + a_2^{(i,j)}$ , reaction 2 happens:  $\mathbf{n}^{(i,j)}(t + \tau^{(i,j)}) = \mathbf{n}^{(i,j)}(t) - [1, 0]^T$
  - if  $a_1^{(i,j)} + a_2^{(i,j)} \leq r_2 a_{\text{sum}}^{(i,j)}$ , reaction 3 happens:  $\mathbf{n}^{(i,j)}(t + \tau^{(i,j)}) = \mathbf{n}^{(i,j)}(t) - [1, 1]^T$

else,  $\mathbf{n}^{(i,j)}(t + \tau^{(i,j)}) = \mathbf{n}^{(i,j)}(t)$
4. Go to the next mesh element.

## B Additional numerical tests

### B.1 Particle-based solution of a PDE

Consider a one-dimensional advection-diffusion PDE on the semi-infinite domain  $\Omega = [0, +\infty)$ ,

$$\begin{cases} \frac{\partial u}{\partial t} + v \frac{\partial u}{\partial x} = D \frac{\partial^2 u}{\partial x^2}, & u(x, t_0) = u_0(x), \\ v u(0, t) + D \frac{\partial u}{\partial x}(0, t) = 0, & u(+\infty, t) = 0, \end{cases} \tag{29}$$

where  $u_0$  is non-zero on a single element of the numerical mesh. This problem can be represented by a stochastic equation with a reflective boundary condition at  $x = 0$ :

$$X^k(t + \Delta t) = X^k(t) + v \Delta t + \sqrt{2D \Delta t} \xi, \tag{30}$$

where  $k = 1, \dots, M$  and  $\xi$  is a standard Gaussian random variable.  $X^k$  is the position of particle  $k$ , driven by Brownian dynamics and velocity  $v$ . Initially at  $t_0 = 0$ , the  $M$  particles are located very close to  $x = 0$  to mimic the Dirac delta point source, i.e.,

$$X^k(0) = \epsilon, \quad \text{where } 0 < \epsilon \ll 1. \tag{31}$$

The Péclet number  $Pe = (v \Delta x)/D$  classifies the system as diffusion-dominated ( $Pe < 1$ ) or advection-dominated ( $Pe \gg 1$ ). For  $D = 10^{-5} \text{ m}^2/\text{s}$  and  $\Delta x = 0.01 \text{ m}$ ,

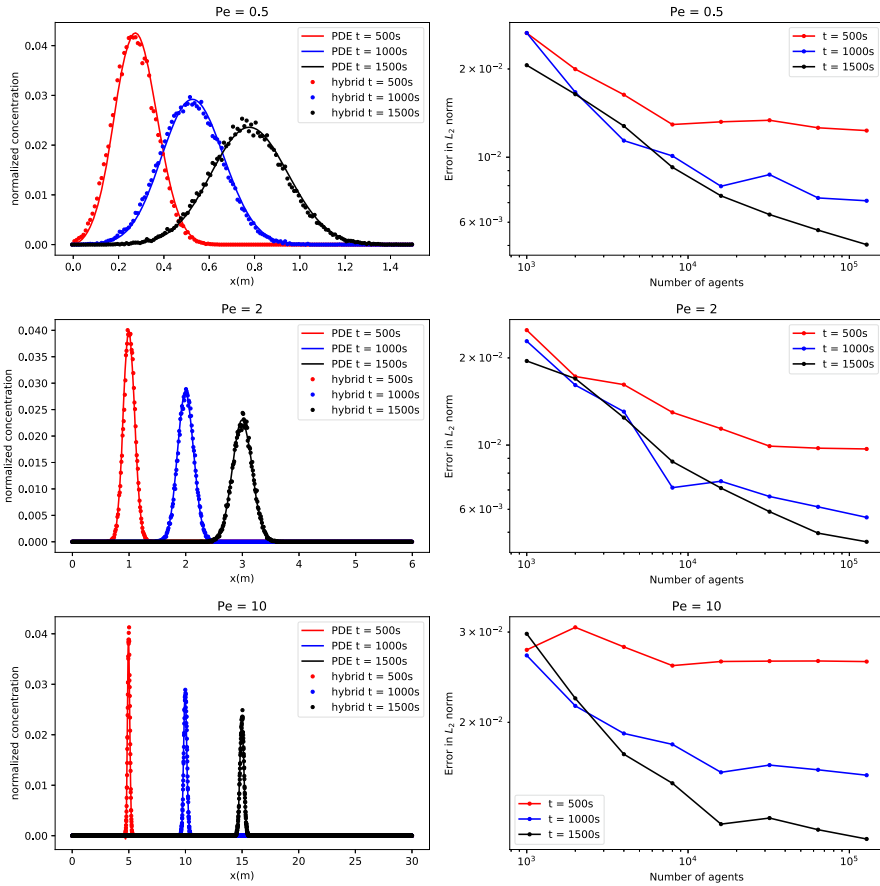


**Fig. 8** Left column: Deterministic and stochastic solutions of (29). Results are shown at  $t = 500$  s, 1000 s, and 1500 s with Péclet numbers  $Pe = 0.5, 2.0$ , and  $10.0$ ; Right column: Model discrepancy  $\epsilon$  at  $t = 500$  s, 1000 s, and 1500 s. The error  $\epsilon$  is plotted in log–log scale as function of the number of particles  $M = 2^p \times 1000$  ( $p = 1, \dots, 8$ ), for Péclet numbers  $Pe = 0.5, 2.0$  and  $10.0$

we vary the velocity  $v$  to get  $Pe = 0.5, 2.0$  and  $10.0$ . Figure 8 provides a comparison between the deterministic and stochastic models. The latter involves  $M = 10,000$  particles; and the number of particles in each mesh element is normalized by  $M$ . Good agreement is observed for a range of Péclet number.

The discrepancy error  $\epsilon$  provides a quantitative comparison between the two models. It is defined as the  $\ell^2$  norm of the difference between their respective solutions,  $\epsilon = [\sum_{i=1}^{N_x} (u_i - U_i)^2]^{1/2}$ . Here  $u_i$  is the deterministic solution at  $x = (i - 0.5)\Delta x$  and  $U_i$  is the normalized number of particles within the  $i$ th mesh element,  $(i - 1)\Delta x \leq x \leq i\Delta x$ . The stochastic simulation is not affected by the mesh size  $\Delta x$ ; the mesh is only used to count the number of particles in each mesh element so that visual comparison can be made. Figure 8 exhibits  $\epsilon$  as function of the number of particles  $M$ , where

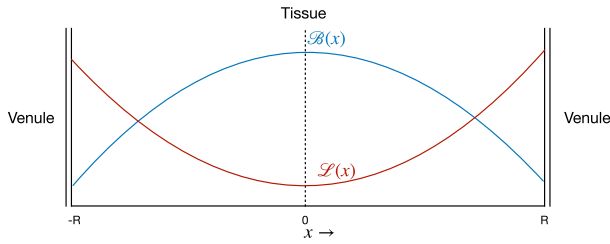


Fig. 9 One-dimensional simulation domain motivated by the Krogh tissue cylinder model

$M = 2^p \times 1000$  with  $p = 1, \dots, 8$ , for various Péclet numbers. As expected, the error decreases with  $M$  in all Pe regimes.

### B.2 One-dimensional simulations

We consider a one-dimensional analog of the Krogh tissue cylinder model (Krogh 1922), in which the tissue is perfused by parallel blood vessels. According to this model, the tissue is composed of cylindrical regions (of radius  $R$ ), such is that each region is fed by a single blood vessel and effectively isolated from the adjacent regions by a cylindrical surface of symmetry. Without loss of generality, we replace the cylindrical domain with a one-dimensional geometry shown in Fig. 9.

As a result, significant mathematical simplifications can be made in the analysis of the model (Keller and Segel 1971). The one-dimensional version of (5) is solved numerically on the spatial domain  $\Omega = [x_{sk}, x_{cap}]$  of length  $R = x_{cap} - x_{sk}$ , where  $x_{sk} = 0$  and  $x_{cap}$  are the locations of the skin and the capillary/venule, respectively.

In the one-dimensional version of the initial and boundary conditions from Sect. 3.5, we set  $h_a = 1$  and  $\mathcal{A}_0 = 10^{-5}$  M, with values of the remaining parameters listed in Table 1.

#### B.2.1 One leukocyte chasing one bacterium

In this numerical experiment, one bacterium is released at  $x_{sk} = 0$  m and one leukocyte at  $x_{cap} = 10^{-4}$  m. The interval  $\Omega$  is divided into 200 mesh elements. This setting provides a simplified representation of a neutrophil chasing a bacterium in the lab (Rogers xxxx). The reaction-rate value in Table 1 is such that neither the leukocyte nor the bacterium grows and/or decays during the time interval  $t \in [0, 1000$  s]. We further assume that, upon encounter (numerically, once they enter the same mesh element), both the bacteria and leukocyte die immediately. To keep a sharper concentration gradient and save the simulation time, we set  $D = 10^{-12}$  m<sup>2</sup>/s in this single test.

Left column of Fig. 10 reveals that the deterministic PDE solution does not provide an accurate description of this experiment. Our hybrid method, on the other hand, accurately captures the microscopic random dynamics of the cells. Right column of Fig. 10 shows one trajectory of the leukocyte “chasing” the bacterium. The Brownian motion of the leukocyte and the bacterium introduces

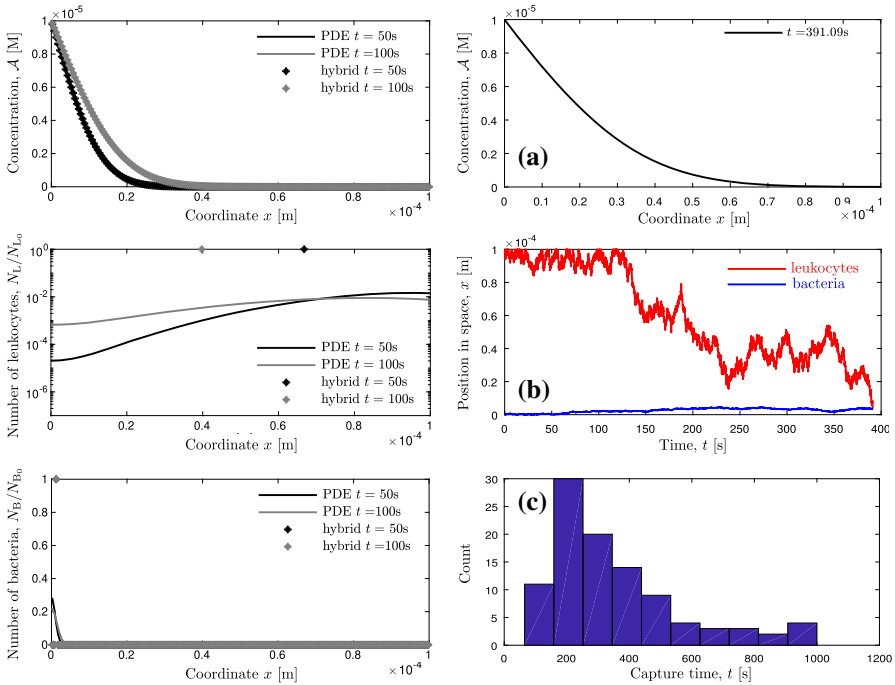


**Fig. 10** A leukocyte chasing a bacterium in one spatial dimension. Left column: the deterministic (solid lines) and hybrid-method (diamonds) solutions at times  $t = 50$  s and 100 s. Right column: **a** the chemoattractant concentration at capture time, **b** representative trajectories of the leukocytes and bacteria up to the capture time, and **c** histogram of the capture times from 100 hybrid one-dimensional simulations

strong stochastic effects in the trajectory, which is naturally absent in the deterministic solution. This is an extreme scenario where different scales invoke the need for different simulation approaches. Concentration, as an average (macroscopic) description generally used for large number of particles, becomes an inadequate quantity to represent the dynamic of single particles (bacterium and leukocyte).

The last frame of Fig. 10 shows the histogram of capture time from 100 hybrid simulations. The average capture time of these 100 simulations is 351.3035 s. Since the leukocyte has less space to move about in one dimension than in two, it captures the bacterium faster.

### B.2.2 Large populations of leukocytes and bacteria

We examine the situation where relatively large numbers of bacteria and leukocytes are involved in the inflammation process. The latter takes place in the domain  $\Omega = [0, 10^{-3} \text{ m}]$ , which is divided into 200 mesh elements. Populations of intermediate size consist of  $N_{L0} = 8000$  leukocytes and  $N_{B0} = 8000$  bacteria. Figure 11 shows two profiles of the chemoattractant concentration and the normalized numbers of bacteria and leukocytes. Predictions of the two methods are similar, except for some

stochastic fluctuations in the numbers of cells. Furthermore, the hybrid method yields more detailed information about the reactions between leukocytes and bacteria than its PDE-based counterpart. The reduction in the population size with time is reported in Fig. 11a, b. During the early stages of inflammation, before leukocytes reach bacteria near the wound, the population-size changes are mostly due to the growth of bacteria and the natural death of leukocytes. Three representative leukocyte trajectories are shown in Fig. 11c.

We repeat this experiment but for large populations of leukocytes and bacteria,  $N_{L0} = N_{B0} = 8 \times 10^5$ . As one would expect, the PDE-based and hybrid models now yield virtually indistinguishable results (Fig. 12). This proves our hybrid method to be accurate as well as flexible for multiscale simulations in multi-species biological systems. Moreover, reactions, population changes and individual cell behavior can be observed on the fly (Fig. 12).

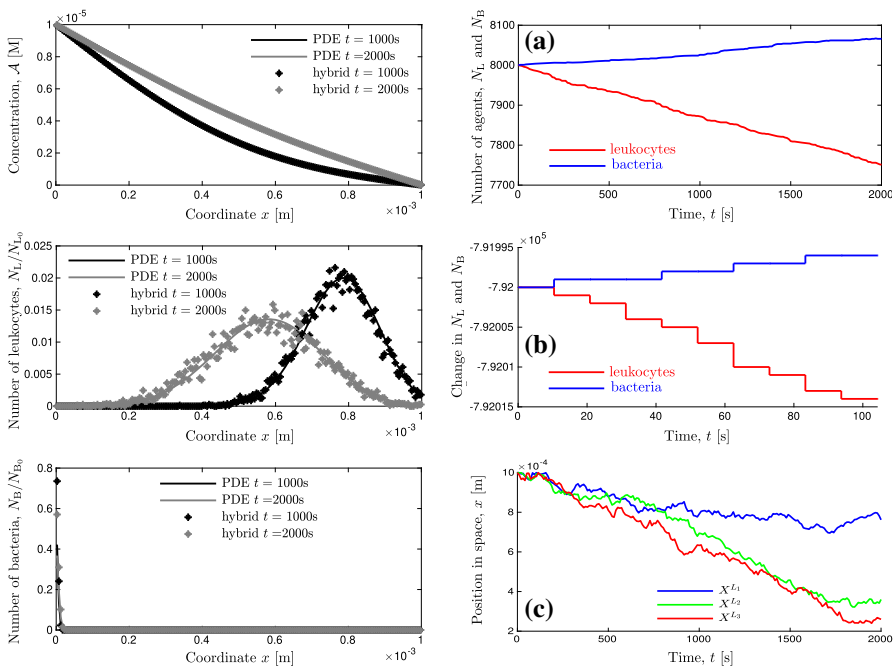


**Fig. 11** One-dimensional deterministic (solid lines) and hybrid (diamonds) simulations of inflammation process with an intermediate-size population of leukocytes ( $N_{L0} = 8000$ ) and bacteria  $N_{B0} = 8000$ . Left column: the solution at times  $t = 1000$  s and  $2000$  s. Right column: **a** change in the size of populations over simulation time, **b** zoomed changes during early times, and **c** trajectories of three randomly selected leukocytes

### B.3 Two-dimensional simulations

#### B.3.1 Small populations of leukocytes and bacteria

Leukocytes enter the tissue from three locations along the blood vessel, as shown in Fig. 3, with the fixed number of leukocytes at each site  $N_{L_1} = 2$ ,  $N_{L_2} = 2$  and  $N_{L_3} = 1$ , respectively. The total of  $N_B = 5$  bacteria invade from the wound. We set  $x_{out} = 4 \times 10^{-4}$  m and  $y_{cap} = 10^{-4}$  m.

The simulation results are presented in Fig. 13 up to time  $t = 1000$  s. The leukocytes disperse over the domain as time goes by, showing strong stochastic dynamics due to motility, but tend to migrate to the wound due to the chemotaxis effects.

#### B.3.2 Large populations of leukocytes and bacteria

The total of  $N_{L_0} = M_B = 8 \times 10^5$  leukocytes enter the tissue from the blood vessel:  $N_{L_1} = 3 \times 10^5$  at  $x_{L_1}$ ,  $N_{L_2} = 3 \times 10^5$  at  $x_{L_2}$  and  $N_{L_3} = 2 \times 10^5$  at  $x_{L_3}$ . The total of  $N_{B_0} = 8 \times 10^5$  invades from the wound. This setting gives rise to the collective

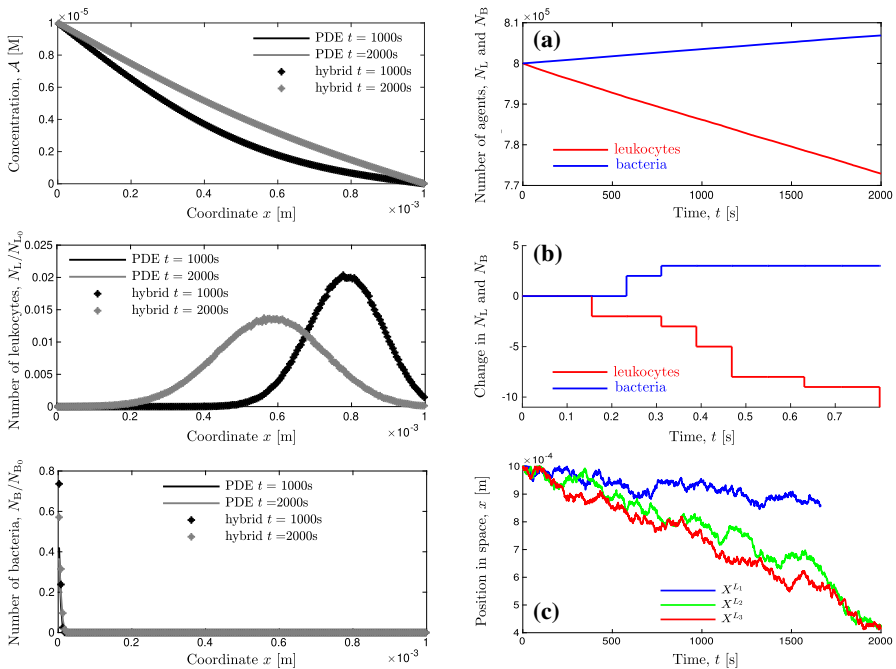


**Fig. 12** One-dimensional deterministic (solid lines) and hybrid (diamonds) simulations of inflammation process with a large population of leukocytes ( $N_{L_0} = 8 \times 10^5$ ) and bacteria  $N_{B_0} = 8 \times 10^5$ . Left column: the solution at times  $t = 1000$  s and 2000 s. Solid lines are the profile of deterministic solution and stars are the hybrid-method results. Right column: **a** change in the size of populations over simulation time, **b** zoomed-in changes during early times, and **c** trajectories of three randomly selected leukocytes



behavior of leukocytes (Fig. 14), in which the random fluctuations observed in the previous section are smoothed out. The normalized particle-number map is less chaotic and smoother than that in Fig. 6. More leukocytes congregate in the left part of the simulation domain than on the right because more of them are released from  $x_{L_1}$  than from  $x_{L_3}$ . This is well understood in terms of diffusion of concentration. The reaction zone is more pronounced in the results for large populations.

The individual behavior of leukocytes has the same pattern as before (Fig. 15). Changes in the population size have the same trends as those observed in the intermediate-size populations. However, the reactions are more intense during the same zoomed-in time interval due to a larger number of leukocytes.

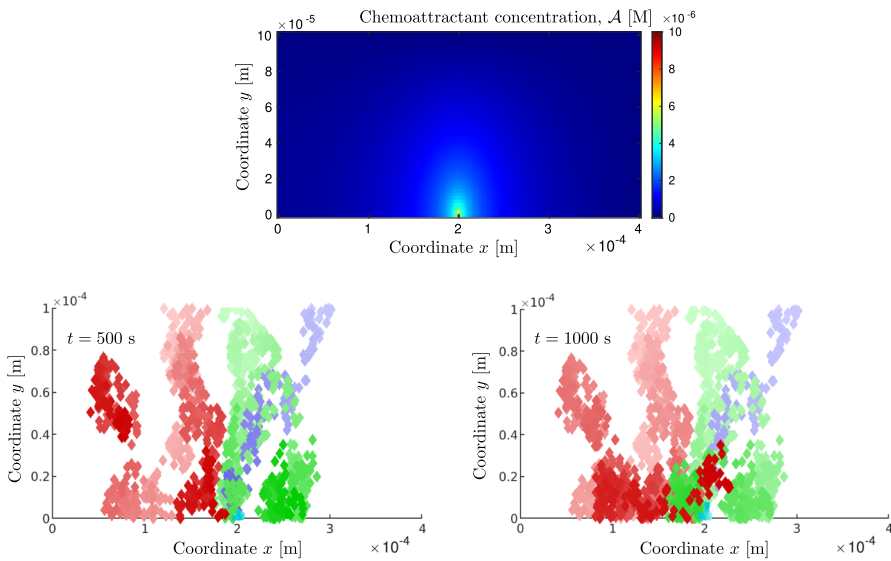


**Fig. 13** Two-dimensional simulations of chemotaxis–motility–reactions of 5 particles. Top row: the chemoattractant concentration,  $\mathcal{A}(\mathbf{x}, t)$ , at  $t = 1000$  s. Bottom row: trajectories of the leukocytes and bacteria at times  $t = 500$  s and  $1000$  s, respectively. The lighter colors represent positions at earlier times, and the darker colors represent positions at later times. Red diamonds are leukocytes released from  $x_{L_1}$ , green diamonds are from  $x_{L_2}$ , blue diamonds are from  $x_{L_3}$ , and cyan diamonds represent bacteria traces

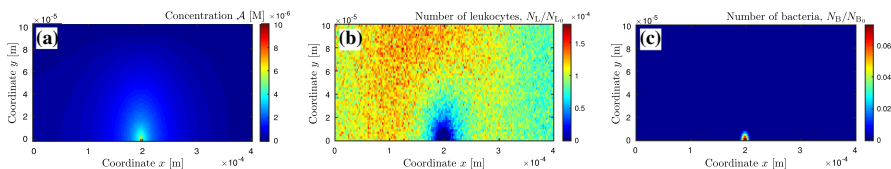


**Fig. 14** Two-dimensional simulations of chemotaxis–motility–reactions of  $8 \times 10^5$  particles. Temporal snapshots, at time  $t = 1000$  s, of **a** the chemoattractant concentration and the numbers of **b** leukocytes and **c** bacteria normalized with their initial population numbers

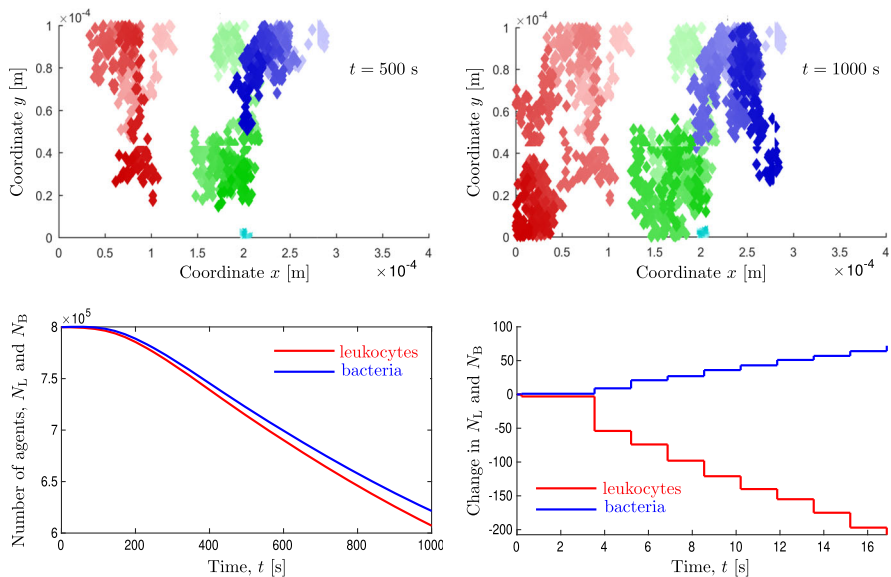


**Fig. 15** Two-dimensional simulations of chemotaxis–motility–reactions of  $8 \times 10^5$  particles. Top row: trajectories of the leukocytes and bacteria at times  $t = 500$  s and 1000 s, respectively. The lighter colors represent positions at earlier times, and the darker colors represent positions at later times. Red diamonds are leukocytes released from  $x_{L1}$ , green diamonds are from  $x_{L2}$ , blue diamonds are from  $x_{L3}$ , and cyan diamonds represent bacteria traces. Bottom row: change in the size of populations over simulation time and zoomed changes during early times

## References

- Alt W (1980) Biased random walk models for chemotaxis and related diffusion approximations. *J Math Biol* 9(2):147–177
- Alt W, Lauffenburger DA (1987) Transient behavior of a chemotaxis system modelling certain types of tissue inflammation. *J Math Biol* 24(6):691–722
- Anderson ARA, Chaplain MAJ (1998) Continuous and discrete mathematical models of tumor-induced angiogenesis. *Bull Math Biol* 60(5):857–899
- Bakarji J, Tartakovsky DM (2017) On the use of reverse Brownian motion to accelerate hybrid simulations. *J Comput Phys* 334:68–80
- Beesley JE, Pearson JD, Carleton JS, Hutchings A, Gordon JL (1978) Interaction of leukocytes with vascular cells in culture. *J Cell Sci* 33(1):85–101
- Bosma TNP, Schnoor JL, Schraa G, Zehnder AJB (1988) Simulation model for biotransformation of xenobiotics and chemotaxis in soil columns. *J Contam Hydrol* 2(3):225–236
- Bravi B, Longo G (2015) The unconventionality of nature: biology, from noise to functional randomness. In: International conference on unconventional computation and natural computation. Springer, pp 3–34
- Chandrasekhar S (1943) Stochastic problems in physics and astronomy. *Rev Mod Phys* 15(1):1
- Changeux J-P, Danchin A (1976) Selective stabilisation of developing synapses as a mechanism for the specification of neuronal networks. *Nature* 264(5588):705–712
- Choi T-J, Maurya MR, Tartakovsky DM, Subramaniam S (2010) Stochastic hybrid modeling of intracellular calcium dynamics. *J Chem Phys* 133(16):165101
- Choi T-J, Maurya MR, Tartakovsky DM, Subramaniam S (2012) Stochastic operator-splitting method for reaction–diffusion systems. *J Chem Phys* 137(18):184102
- Dallon JC, Othmer HG (1997) A discrete cell model with adaptive signalling for aggregation of *Dicystostelium discoideum*. *Philos Trans R Soc Lond B* 352(1351):391–417

- Dallon JC, Othmer HG (2004) How cellular movement determines the collective force generated by the *Dictyostelium discoideum* slug. *J Theor Biol* 231(2):203–222
- Darwin C (1859) On the origins of species. John Murray, London
- Deisboeck TS, Wang Z, Macklin P, Cristini V (2011) Multiscale cancer modeling. *Annu Rev Biomed Eng* 13:127–155
- Di Costanzo E, Menci M, Messina E, Natalini R, Vecchio A (2019) A hybrid model of collective motion of discrete particles under alignment and continuum chemotaxis. *Discrete Contin Dyn Syst B* 22(11):443–472
- Farrell BE, Daniele RP, Lauffenburger DA (1990) Quantitative relationships between single-cell and cell-population model parameters for chemosensory migration responses of alveolar macrophages to C5a. *Cell Motil Cytoskeleton* 16(4):279–293
- Fehr J, Jacob HS (1977) In vitro granulocyte adherence and in vivo margination: two associated complement-dependent functions. *J Exp Med* 146(3):641–652
- Gillespie DT (1976) A general method for numerically simulating the stochastic time evolution of coupled chemical reactions. *J Comput Phys* 22(4):403–434
- Gillespie DT (1992) A rigorous derivation of the chemical master equation. *Phys A* 188:404–425
- Guo Z, Sliot PMA, Tay JC (2008) A hybrid agent-based approach for modeling microbiological systems. *J Theor Biol* 255(2):163–175
- Hillen T, Painter KJ (2009) A user's guide to PDE models for chemotaxis. *J Math Biol* 58(1–2):183
- Hoang AN, Jones CN, Dimisko L, Hamza B, Martel J, Kojic N, Irimia D (2013) Measuring neutrophil speed and directionality during chemotaxis, directly from a droplet of whole blood. *Technology* 1(01):49–57
- Hundsdoerfer W, Verwer JG (2013) Numerical solution of time-dependent advection–diffusion–reaction equations, vol 33. Springer, Berlin
- Keller EF, Segel LA (1971) Model for chemotaxis. *J Theor Biol* 30(2):225–234
- Krogh A (1922) The anatomy and physiology of capillaries, vol 18. Yale University Press, London
- Lauffenburger D, Keller KH (1979) Effects of leukocyte random motility and chemotaxis in tissue inflammatory response. *J Theor Biol* 81(3):475–503
- LeVeque RJ (2002) Finite volume methods for hyperbolic problems, vol 31. Cambridge University Press, Cambridge
- Lowengrub JS, Frieboes HB, Jin F, Chuang Y-L, Li X, Macklin P, Wise SM, Cristini V (2009) Nonlinear modelling of cancer: bridging the gap between cells and tumours. *Nonlinearity* 23(1):R1
- Munsky B, Khammash M (2006) The finite state projection algorithm for the solution of the chemical master equation. *J Chem Phys* 124:044104
- Othmer HG, Hillen T (2002) The diffusion limit of transport equations II: Chemotaxis equations. *SIAM J. Appl. Math.* 62(4):1222–1250
- Rivero MA, Tranquillo RT, Buettner HM, Lauffenburger DA (1989) Transport models for chemotactic cell populations based on individual cell behavior. *Chem Eng Sci* 44(12):2881–2897
- Rodríguez JV, Kaandorp JA, Dobrzyński M, Blom JG (2006) Spatial stochastic modelling of the phosphoenolpyruvate-dependent phosphotransferase (PTS) pathway in *Escherichia coli*. *Bioinformatics* 22(15):1895–1901
- Rogers D, Movie–neutrophil chasing bacteria. [https://embryology.med.unsw.edu.au/embryology/index.php/Movie\\_-\\_Neutrophil\\_chasing\\_bacteria](https://embryology.med.unsw.edu.au/embryology/index.php/Movie_-_Neutrophil_chasing_bacteria)
- Ruiz-Martinez A, Bartol TM, Sejnowski TJ, Tartakovsky DM (2019) Stochastic self-tuning hybrid algorithm for reaction–diffusion systems. *J Chem Phys* 151(24):244117
- Saad Y, Schultz MH (1986) GMRES: a generalized minimal residual algorithm for solving nonsymmetric linear systems. *SIAM J Sci Stat Comput* 7(3):856–869
- Strang G (1968) On the construction and comparison of difference schemes. *SIAM J Numer Anal* 5(3):506–517
- Su B, Zhou W, Dorman KS, Jones DE (2009) Mathematical modelling of immune response in tissues. *Comput Math Methods Med* 10(1):9–38
- Taverniers S, Tartakovsky DM (2017) A tightly-coupled domain-decomposition approach for highly nonlinear stochastic multiphysics systems. *J Comput Phys* 330:884–901
- Tranquillo RT, Lauffenburger DA (1990) Definition and measurement of cell migration coefficients. In: Alt W, Hoffmann G (eds) Biological motion, vol 89. Lecture notes in biomathematics. Springer, Heidelberg, pp 475–486
- Tyson R, Stern LG, LeVeque RJ (2000) Fractional step methods applied to a chemotaxis model. *J Math Biol* 41(5):455–475

- Walker HK, Hall WD, Hurst JW (1990) *The oral cavity and associated structures-clinical methods: the history, physical, and laboratory examinations*. Butterworths, London
- Ward ND, Falle S, Olson MS (2011) Modeling chemotactic waves in saturated porous media using adaptive mesh refinement. *Transp Porous Media* 89(3):487–504
- Zigmond SH (1977) Ability of polymorphonuclear leukocytes to orient in gradients of chemotactic factors. *J Cell Biol* 75(2):606–616
- Zigmond SH (1981) Consequences of chemotactic peptide receptor modulation for leukocyte orientation. *J Cell Biol* 88(3):644–647

**Publisher's Note** Springer Nature remains neutral with regard to jurisdictional claims in published maps and institutional affiliations.